





Cite this: *RSC Adv.*, 2024, 14, 4424

# Effect of copper doping on the photocatalytic performance of Ni<sub>2</sub>O<sub>3</sub>@PC membrane composites in norfloxacin degradation

Anastassiya A. Mashentseva, <sup>ab</sup> Dinara T. Nurpeisova <sup>\*c</sup> and Murat Barsbay <sup>d</sup>

In this study, copper (Cu) and nickel oxide (Ni<sub>2</sub>O<sub>3</sub>) microtubes (MTs) were synthesized using an electroless template deposition technique within porous polycarbonate (PC) track-etched membranes (TeMs) to obtain Cu@PC and Ni<sub>2</sub>O<sub>3</sub>@PC composite membranes, respectively. The pristine PC TeMs featured nanochannels with a pore density of  $4 \times 10^7$  pores per cm<sup>2</sup> and an average pore diameter of  $400 \pm 13$  nm. The synthesis of a mixed composite, combining Cu and Ni<sub>2</sub>O<sub>3</sub> within the PC matrix, was achieved through a two-step deposition process using a Ni<sub>2</sub>O<sub>3</sub>@PC template. An analysis of the resultant composite structure (Cu/Ni<sub>2</sub>O<sub>3</sub>@PC) confirmed the existence of CuNi (97.3%) and CuO (2.7%) crystalline phases. The synthesized catalysts were characterized by scanning electron microscopy (SEM), energy dispersive X-ray spectroscopy (EDX), X-ray diffraction (XRD) analysis, and atomic force microscopy (AFM). In photodegradation assessments, the Cu/Ni<sub>2</sub>O<sub>3</sub>@PC mixed composite demonstrated higher photocatalytic activity, achieving a substantial 59% degradation of norfloxacin (NOR) under UV light irradiation. This performance surpassed that of both Ni<sub>2</sub>O<sub>3</sub>@PC and Cu@PC composites. The optimal pH for maximum NOR removal from the aqueous solution was determined to be pH 5, with a reaction time of 180 min. The degradation of NOR in the presence of these composites adhered to the Langmuir–Hinshelwood mechanism and a pseudo-first order kinetic model. The reusability of the catalysts was also investigated for 10 consecutive runs, without any activation or regeneration treatments. The Cu@PC membrane catalyst demonstrated a marked decline in degradation efficiency after the 2nd test cycle, ultimately catalyzing only 10% of NOR after the 10th cycle. In contrast, the Ni<sub>2</sub>O<sub>3</sub>@PC based catalyst demonstrated a more stable NOR degradation efficiency throughout all 10 runs, with 27% NOR removal observed during the final test. Remarkably, the catalytic performance of the Cu/Ni<sub>2</sub>O<sub>3</sub>@PC mixed composite remained highly active even after being recycled 4 times. The degradation efficiency exhibited a gradual reduction, with a 17% decrease after the 6th run and a cumulative 35% removal of NOR achieved by the 10th cycle. Overall, the findings indicate that Cu/Ni<sub>2</sub>O<sub>3</sub>@PC mixed composite membranes may represent an advancement in the quest to mitigate the adverse effects of antibiotic pollution in aquatic environments and hold significant promise for sustainable water treatment practices.

Received 2nd November 2023  
Accepted 26th January 2024

DOI: 10.1039/d3ra07471d

rsc.li/rsc-advances

## 1. Introduction

Antibiotics have been extensively used in both human and veterinary medicines for various purposes.<sup>1</sup> Usually, antibiotics cannot completely metabolize in the body and are excreted *via* urine and feces and transported to the wastewater treatment plants.<sup>2</sup> Owing to their pervasive use and environmental persistence, antibiotics have become emerging pollutants.<sup>1,3</sup>

Various sources contribute to antibiotic pollution in the environment, with primary origins stemming from medical treatments, agricultural practices, livestock farming, and industrial production.<sup>4</sup> Notably, approximately 11.2 million kg of antibiotics are annually administered in livestock farming.<sup>5</sup> Due to the limited capacity of wastewater treatment plants to remove antimicrobials, the exceeding presence of antibiotics in environmental pollutants poses the risk of generation and spread of antimicrobial-resistant bacteria and resistance genes.<sup>6–8</sup> Fluoroquinolones, a commonly used class of broad-spectrum antibiotics with good oral bioavailability in human and veterinary medicine for treating urinary tract infections, pneumonia, gastroenteritis and gonococcal infections have become the most frequently detected antibiotics in diverse water bodies, such as rivers, domestic sewage and hospital effluent.<sup>9–11</sup> This is

<sup>a</sup>The Institute of Nuclear Physics of the Republic of Kazakhstan, 050032 Almaty, Kazakhstan

<sup>b</sup>Department of Nuclear Physics, New Materials and Technologies, L.N. Gumilyov Eurasian National University, 010008 Astana, Kazakhstan

<sup>c</sup>Department of Chemistry, L.N. Gumilyov Eurasian National University, 010008 Astana, Kazakhstan. E-mail: nurpeisova\_dt\_1@enu.kz

<sup>d</sup>Department of Chemistry, Hacettepe University, 06800 Ankara, Turkey


attributed to their low degree of metabolizing in living organisms, typically around 15–20%.<sup>12,13</sup>

Antibiotic-contaminated wastewater and natural waters pose serious risks to human and animal health when they enter the food chain. Additionally, they significantly increase the resistance of bacteria in water bodies and suppress or kill certain beneficial bacteria in natural ecosystems.<sup>14</sup> Many conventional strategies have been employed to remove antibiotic residuals from aqueous environments such as biodegradation, sand filtration, coagulation, electrolysis, ultraviolet (UV) radiation, membrane filtration, sedimentation.<sup>15,16</sup> Nonetheless, each method has certain limitations in its application and is usually restricted by technical and economic challenges. Furthermore, these methods suffer from shortcomings like incomplete antibiotic removal, substantial energy costs, formation of toxic sludge or waste that requires proper disposal.<sup>17</sup>

As an alternative to the aforementioned techniques, advanced oxidation processes (AOPs) are noteworthy, particularly those involving semiconductor photocatalysts.<sup>1,18</sup> These processes rely on catalytic photodegradation of organic pollutants in aqueous solution and exhibit superior efficiency compared to conventional methods while being environmentally friendly.<sup>19,20</sup> Adsorption is also efficient for the removal of antibiotics micropollutants. However, even highly effective adsorbent like activated carbon or Metal–Organic Frameworks (MOFs) cannot entirely solve the issue, as most adsorbents are not reusable, and regeneration techniques are complex and expensive.<sup>21</sup> Heterogeneous photocatalysis proves to be an effective solution for addressing the issue of antibiotics, particularly when operating in acidic pH conditions. Numerous studies have explored the removal rates of pharmaceuticals in acidic conditions using different materials. For instance, mesoporous silica SBA-15 demonstrated high removal efficiency for various pharmaceuticals, including carbamazepine, diclofenac, ibuprofen, ketoprofen, and clofibrate acid, in acidic media (pH 3–5).<sup>22</sup> Volcanic sand was utilized in heterogeneous catalytic ozonation, leading to enhanced removal of ketoprofen, naproxen, and cimetidine at pH 4.0.<sup>23</sup> In another study, pH 5.5 was identified as the optimal condition for efficiently removing a range of micropollutant, such as endocrine disruptors, pharmaceuticals, personal care products, and perfluorinated compounds, using an iron-impregnated zeolite catalyst.<sup>24</sup>

Ni-based nanocomposites possess great prospects for practical applications, particularly in water purification processes. Electrochemically deposited Ni nanotubes on various supports have been intensively studied,<sup>25</sup> demonstrating their potential in catalytic,<sup>26,27</sup> biomedical<sup>28,29</sup> and sensors<sup>30</sup> applications. The electroless deposition technique has also been applied for synthesis of hollow nickel or nickel oxide nanotube arrays, highlighting their excellent catalytic and conductive properties.<sup>31–33</sup> Incorporation of metallic nanoparticles on the surface of Ni substrate has been shown to enhance storage capacity, charge separation, and photocatalytic activity of the resulting heterostructures.<sup>34–37</sup>

In this study, we present the galvanic replacement of initially electrolessly deposited Ni<sub>2</sub>O<sub>3</sub> microtubes (MTs) within the pores

of polycarbonate (PC) track-etched membranes (TeMs) with NiCu MTs. The application of polymeric TeMs as a support for composites synthesis has proven effective in producing highly efficient membrane catalysts for the removal of different classes of contaminants.<sup>38–41</sup> We conducted comprehensive investigations on both the initial (Cu@PC and Ni<sub>2</sub>O<sub>3</sub>@PC) and the resulting (Cu/Ni<sub>2</sub>O<sub>3</sub>@PC) composites, focusing on their photocatalytic degradation capacity for norfloxacin (NOR).

## 2. Materials and methods

### 2.1. Materials

Copper nitrate pentahydrate, nickel sulfate hexahydrate, ascorbic acid, sodium hypophosphite, palladium chloride, tin chloride, norfloxacin were purchased from Sigma Aldrich and used without additional purification. Throughout all experiments, aqueous solutions were prepared using deionized water (18.2 Mohm cm<sup>−1</sup>, Aquilion – D301, Aquilion JSC).

### 2.2. Irradiation and track-etching of PC films

To obtain track-etched membranes, a PC Makrofol KG film with the thickness of 20 μm (Bayer, Germany) was used. The film was irradiated with <sup>84</sup>Kr<sup>15+</sup> ions at a specific energy (1.3 MeV per nucleon) and fluency using a cyclotron (Cyclotron DC-60, Institute of Nuclear Physics of Kazakhstan). After irradiation, the film was etched for 75 s in 6.0 M NaOH to attain PC TeMs with nanochannels of an average pore diameter of 400 ± 13 nm and a pore density of 4 × 10<sup>7</sup> pores per cm<sup>2</sup>. Samples were stored under ambient conditions at room temperature.

### 2.3. Synthesis of composite TeMs

Before the electroless deposition process, all PC TeMs were treated in sensitization and activation solutions. Sensitization involved rinsing the samples in a solution containing 50 g L<sup>−1</sup> SnCl<sub>2</sub> and 60 mL L<sup>−1</sup> HCl (37%) for 6 min, followed by thorough washing with water for 2–3 min. Subsequently, the sensitized PC TeM sample was activated by immersing it in a solution containing 0.1 g L<sup>−1</sup> PdCl<sub>2</sub> and 10 mL L<sup>−1</sup> HCl (37%) for 6 min.<sup>42</sup> For the synthesis of Ni<sub>2</sub>O<sub>3</sub>@PC and Cu@PC composites, the activated PC TeM sample was placed in a plating solution heated to the desired temperature. After the deposition process was completed, the composite was washed with deionized water and then dried in an oven at 60 °C for 20 min. In order to obtain a mixed composite, referred to as Cu/Ni<sub>2</sub>O<sub>3</sub>@PC, the Ni<sub>2</sub>O<sub>3</sub>@PC composite was used as the initial template. It was placed in a deposition solution containing Cu(SO<sub>4</sub>) and was subsequently reduced by ascorbic acid. The conditions outlined in Table 1 were applied to prepare the Cu@PC composite. The amount of metallic catalyst deposit within the membrane template (mg cm<sup>−2</sup>) was determined gravimetrically, based on the difference in composite mass before and the after the process, with an accuracy of ±0.01 mg (AND BM-252 G by AND, Japan).



Table 1 Experimental details of the synthesis of composite TeMs

Composite	Plating bath composition	Plating conditions			
		pH	<i>T</i> , °C	Plating time, min	Ref.
Cu@PC	CuSO <sub>4</sub> ·5H <sub>2</sub> O—9.6 g L <sup>-1</sup> ; CH <sub>3</sub> COOH—10.0 mL L <sup>-1</sup> ; ascorbic acid—8.2 g L <sup>-1</sup>	pH = 4.0 (9.0 M KOH)	25	480.0	47
Ni <sub>2</sub> O <sub>3</sub> @PC	NiSO <sub>4</sub> ·6H <sub>2</sub> O: 55.6 g L <sup>-1</sup> ; NaH <sub>2</sub> PO <sub>2</sub> : 22.0 g L <sup>-1</sup>	2.68	80	1.0	This study
Cu/Ni <sub>2</sub> O <sub>3</sub> @PC	Ni <sub>2</sub> O <sub>3</sub> @PC composite was used as a template, CuSO <sub>4</sub> ·5H <sub>2</sub> O—9.6 g L <sup>-1</sup> ; CH <sub>3</sub> COOH—10.0 mL L <sup>-1</sup> ; ascorbic acid—8.2 g L <sup>-1</sup>	pH = 4.0 (9.0 M KOH)	25	60.0	

#### 2.4. Analysis of the structure and composition of composite membranes

The pore size of the initial template and the structural parameters of the MTs were determined by porometry method, using the Hagen–Poiseuille eqn (1):<sup>43</sup>

$$Q = \frac{8\pi}{3MRT} \sqrt{\frac{nr^3\Delta p}{l}} \quad (1)$$

where  $\Delta p$  is the pressure difference, MPa;  $M$  is the molecular mass of the gas, dyn cm<sup>-2</sup>;  $R$  is the universal gas constant, erg (mol<sup>-1</sup> K<sup>-1</sup>);  $n$  is the number of microtubes per square centimeter of membrane area (template pore density);  $l$  is the membrane thickness, cm; and  $T$  is the temperature, K.

Morphological assessments and dimensional measurements of the resulting composites were performed using a Phenom ProX Desktop scanning electron microscope (SEM) (Thermo Scientific, MA, USA). Energy-dispersive X-ray spectroscopy (EDX) measurements were carried out using a Hitachi TM3030 (Hitachi Ltd, Chiyoda, Tokyo, Japan) microscope equipped with a Bruker XFlash MIN SVE (Bruker, Karlsruhe, Germany) microanalysis system at an accelerating voltage of 15 kV.

The crystal structure of the deposited nanoparticles was examined using a D8 Advance diffractometer (Bruker, Karlsruhe, Germany) in the angular range of  $2\theta$  30–80° with a step of  $2\theta = 0.02^\circ$  (measuring time: 1 s, tube mode: 40 kV, 40 mA). The mean size of crystallites was determined by analyzing the broadening of X-ray diffraction reflections using the Scherer formula.<sup>44</sup> The phase composition was determined using the Rietveld method, which is based on approximating the areas of the diffraction peaks and determining the convergence with reference values for each phase. The volume fraction of the composite phase was determined using eqn (2):<sup>45</sup>

$$V_{\text{admixture}} = \frac{RI_{\text{phase}}}{I_{\text{admixture}} + RI_{\text{phase}}} \quad (2)$$

where  $I_{\text{phase}}$  is the average integral intensity of the main phase of the diffraction line,  $I_{\text{admixture}}$  is the average integral intensity of the additional phase, and  $R$  is the structural coefficient equal to 1.

The surface morphology of the composite membranes was studied using a scanning probe microscope (SmartSPM-1000, NT-MDT, Novato, CA, USA) in semi-contact mode. An NSG10 rectangular-shaped silicon cantilever (length  $95 \pm 5$  μm, width

$30 \pm 5$  μm, thickness 1.5–2.5 μm, probe tip radius = 10 nm, resonance frequency = 200 kHz) TipsNano (Tallinn, Estonia) was employed for this purpose. An initial scan of a  $10 \times 10$  μm<sup>2</sup> sample area was performed at a speed of 5.0 μm s<sup>-1</sup>. The average roughness was calculated based on a scanning area of  $3 \times 3$  μm<sup>2</sup>. The data obtained were processed and analyzed using IAPro software (version 3.2.2., 2012, NT-MDT, Novato, CA, USA).

The determination of the surface charge of the adsorbent based on pH values was carried out by studying the  $\text{pH}_{\text{zpc}}$  (point of zero charge) value across the pH range from 3.0 to 8.0, following the method described in ref. 46. For this, 10 mL of a 0.01 M NaCl solution was adjusted to the desired pH value ( $\text{pH}_i$ ) using 0.1 M HCl(aq) or NaOH(aq). Subsequently,  $1 \times 1$  cm of composite membranes was added to each flask and agitated on a shaker for 24 h at room temperature. Afterward, the final pH value ( $\text{pH}_f$ ) of the resulting filtrate was measured.

#### 2.5. Photocatalytic decomposition of NOR

To study the photocatalytic degradation of NOR, composite PC TeMs sized  $2 \times 2$  cm<sup>2</sup> were placed in 50 mL of 10 mg L<sup>-1</sup> antibiotic solution. The solution was then intensively stirred in the dark for 60 min to establish a “catalyst-antibiotic” adsorption equilibrium. All catalytic experiments were carried out in 200 mL double-wall glassware under UV-light (15 W, 295 nm, Ultra-Vitalux 300 W, Osram, Augsburg, Germany). The distance from the light source to the solution was 20 cm. An aliquot of the reaction mixture with a volume of 1.0 mL was taken every 30 min and measured on a Specord-250 spectrophotometer (Jena Analytic, Jena, Germany) in the wavelength range of 200–400 nm. The effect of pH on the degradation efficiency of NOR was evaluated over the pH range of 3–8 at 40 °C, while other conditions remained consistent with those previously described (pH adjustments were made with 0.1 M NaOH or 0.1 M HCl).

The degradation of NOR was determined based on its characteristic peak at 275 nm, using the following eqn (3):

$$D = \frac{C_0 - C}{C_0} \times 100\% = \frac{A_0 - A}{A_0} \times 100\% \quad (3)$$

where  $A_0$  is the initial absorbance of NOR-containing solution at 275 nm before adding the composite catalyst,  $A$  is the absorbance at 275 nm at different time intervals, and  $C_0$  is the concentration of the feed solution.





### 3. Results and discussions

#### 3.1. Characterization of the catalyst membrane

The electroless template deposition technique represents an elegant and straightforward approach for creating ordered arrays of hollow nanostructures. The galvanic replacement reaction is widely used not only for the synthesis of nanocrystals with hollow and core-shell nanoarchitectures<sup>48</sup> but is also applied in the fabrication of multicomponent functional materials.<sup>38,49,50</sup>

In the cross-sectional SEM images of the pristine  $\text{Ni}_2\text{O}_3@\text{PC}$  composite shown in Fig. 1a–c, one can clearly observe the complete and uniform metal coating of the PC template. The accumulation of deposited nanoparticles on the membrane surface is clearly visible as an abundant phase that covers the entire surface of PC TeMs (Fig. 1d–f), extending into the interior of the nanochannels. In the case of  $\text{Cu}@\text{PC}$ , the morphology of the microtube walls is somewhat less smooth and partially consists of separated copper nanoclusters. The successful synthesis of the  $\text{Cu}/\text{Ni}_2\text{O}_3@\text{PC}$  on the  $\text{Ni}_2\text{O}_3@\text{PC}$  surface is visually indicated by a noticeable change in colour, turning from the original grey to brownish-red. Both the surface and inner surface of the nanochannels in the mixed composite are decorated with spherical copper nanoclusters as seen in Fig. 1c.

The energy-dispersive X-ray analysis (EDX), as presented in Fig. 2, reveals the composition of the pristine samples, where intense carbon and oxygen peaks signify the polymeric PC matrix. The presence of nickel and copper peaks corresponds to the active phase. Additionally, the EDX mappings of the synthesized samples illustrate the presence and uniform distribution of all detectable elements on the membrane surface. Minor peaks of phosphorus (approximately 1.5%) were also detected in the EDX spectra of nickel-containing samples, likely attributed to the use of sodium hypophosphite during the

deposition process. The presence of copper element in the SEM mapping image of the mixed composite confirms the successful deposition of copper onto the  $\text{Ni}_2\text{O}_3@\text{PC}$  substrate.

The data regarding the structural parameters of the resulting composites, including microtube wall thickness determined using eqn (1) and the loading of the active catalyst phase per unit area, are presented in Table 2. Based on the obtained data, the wall thickness of the copper microtubes (MTs) was measured to be  $75.6 \pm 7.4$  nm. Following the subsequent deposition stage, the wall thickness of the mixed composite was calculated to be  $103.8 \pm 3.2$  nm. The deposition rate ( $R$ ) of the electroless deposition process was expressed as the weight gain per  $1 \text{ cm}^2$  of PC TeMs per unit time during the deposition. The high deposition rate of the nickel-plating solution ( $70.65 \text{ mg cm}^{-2} \text{ h}^{-1}$ ) facilitated the deposition of MTs with a wall thickness of  $63.4 \pm 2.3$  nm in just 60 seconds.

X-ray diffraction (XRD) analysis was carried out to identify the structural characteristics of the synthesized catalysts (see Table 2). The X-ray diffractogram of the pristine  $\text{Ni}_2\text{O}_3@\text{PC}$  composite (Fig. 3a) reveals a distinct diffraction peak corresponding to the (102) plane of the  $\text{Ni}_2\text{O}_3$  phase at a  $2\theta$  value of  $39.035^\circ$  (102), and this identified plane closely matches the PDF-00-014-0481 card, indicating a hexagonal structure with symmetry group  $P(0)$ . A minor peak at a  $2\theta$  value of  $36.80^\circ$  can be attributed to the (202) phase, as previously demonstrated in ref. 51.

According to the X-ray diffraction data, the unit cell of the  $\text{Cu}@\text{PC}$  composite is characterized by a cubic symmetry ( $Fm3m$ ) with a cell parameter of 3.608, closely matching the reference value ( $a = 3.6150$ , PDF-03-065-9026). Additionally, a peak around  $2\theta = 38.65^\circ$  is evident in the  $\text{Cu}@\text{PC}$  XRD pattern, attributed to the  $\text{CuO}$  phase (111 plane, PDF card #01-080-1916), which appeared due the oxidation of copper. This observation aligns with findings from similar studies.<sup>52–54</sup> Copper is highly

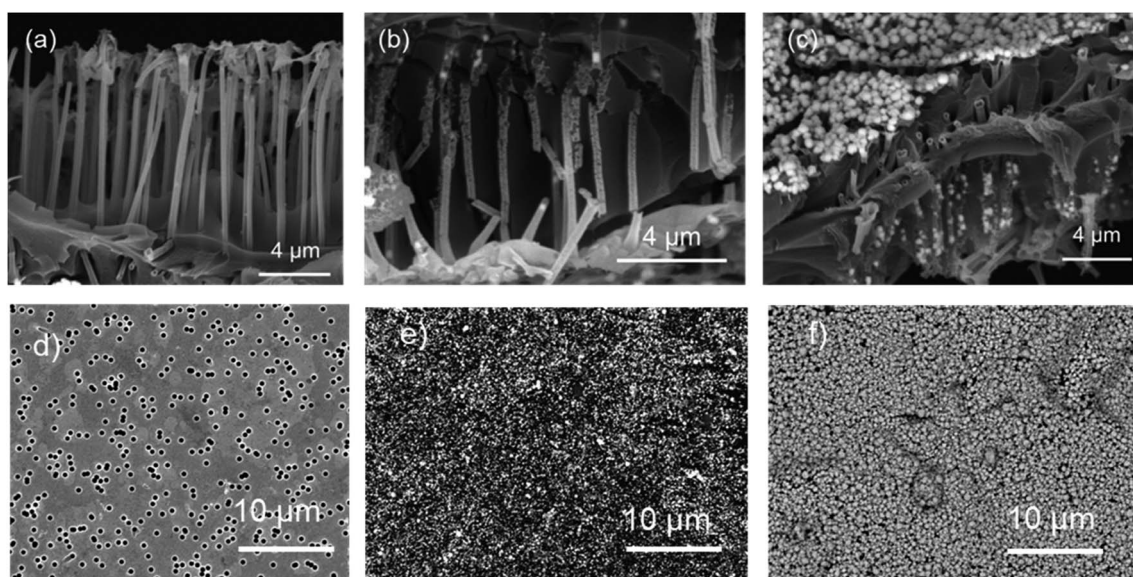


Fig. 1 Electron cross-sectional microphotographs of the studied composite membranes (a)  $\text{Ni}_2\text{O}_3@\text{PC}$ , (b)  $\text{Cu}@\text{PC}$ , (c)  $\text{Cu}/\text{Ni}_2\text{O}_3@\text{PC}$ . Corresponding SEM images of the membrane surfaces (d)  $\text{Ni}_2\text{O}_3@\text{PC}$ , (e)  $\text{Cu}@\text{PC}$ , (f)  $\text{Cu}/\text{Ni}_2\text{O}_3@\text{PC}$ .

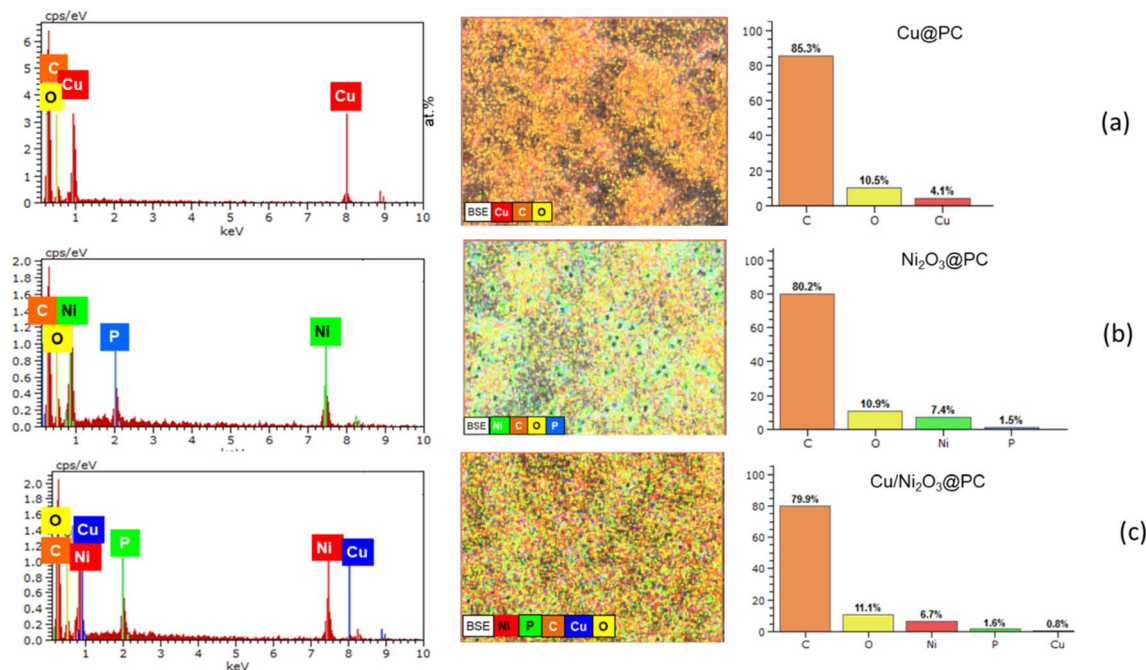


Fig. 2 EDX spectra, elemental mappings, and corresponding atomic percentages of the synthesized composite TeMs: (a) Cu@PC, (b) Ni<sub>2</sub>O<sub>3</sub>@PC, (c) Cu/Ni<sub>2</sub>O<sub>3</sub>@PC.

sensitive to air, and its oxide phases are thermodynamically more stable, leading to the inevitable formation of a surface oxide layer on copper nanoparticles. These results, in agreement with previous studies,<sup>47</sup> confirm the presence of the defined crystalline phases within the composite catalysts. This confirmation is crucial for ensuring their consistent and efficient performance in the degradation of NOR.

The X-ray diffraction pattern of Cu-doped mixed Cu/Ni<sub>2</sub>O<sub>3</sub>@PC composite (Fig. 3b) exhibits a series of the diffraction peaks at  $2\theta$  values of 43.42°, 50.58°, 74.28°, 89.94° and 95.31°, indicating the presence of a face-centered cubic structure of the Ni-Cu alloy (PDF 00-047-1406).<sup>53</sup> Additionally, the peak at 38.95° confirms the presence of copper(II) oxide (CuO) (PDF-01-080-1916) phase. Apparently, the formation of a minor CuO phase (2.7%) on the Cu-Ni alloys is influenced by the solid-state interdiffusion of Cu and O atoms, leads to the creation of an extended diffusion layer that is depleted of electronegative elements.<sup>56</sup>

The average size of crystallites, calculated using the Scherer equation, was found to be 36.7 for Ni<sub>2</sub>O<sub>3</sub>@PC, 23.1 ± 6 for Cu@PC, 33.5 ± 5 and 31.36 nm for the CuNi and CuO phases in Cu/Ni<sub>2</sub>O<sub>3</sub>@PC composite, respectively. The degree of crystallinity (DC) was determined by approximating the values of the full width at half maximum (FWHM) lines using symmetric pseudo-Voigt functions and was found to be 43.8% and 60.5 for initial Ni<sub>2</sub>O<sub>3</sub>@PC and Cu@PC composites, while mixed composite demonstrated a higher DC of 64.2%.

The absorption of radiation by catalysts is crucial for their photocatalytic performance. The UV-Vis diffuse reflectance spectroscopy (DRS) technique was used to measure the optical absorption properties of the synthesized composites (Fig. 4a).

The obtained spectra indicate that the Cu@PC composite exhibits enhanced absorptive capacity in both the visible and UV light regions. On the other hand, Ni<sub>2</sub>O<sub>3</sub>@PC primarily absorbs UV light (below 400 nm). The formation of the solid solution phase (SSS) of CuNi in the mixed composite significantly improves the optical capabilities of the photocatalyst, resulting in a more robust and responsive absorption of UV light. To calculate the band gap energy, data from the UV-vis DRS measurements of the membrane composites were used to construct a Tauc plot using eqn (4):

$$\alpha = \frac{A(h\nu - E_g)^n}{h\nu} \quad (4)$$

where  $\alpha$  is the absorption coefficient,  $A$  is a constant,  $E_g$  is the absorption band gap energy,  $h\nu$  is the photon energy, and  $n$  depends on the nature of the transition. It can be 1/2, 2, 3/2, or 3, corresponding to allowed direct, allowed indirect, forbidden direct, and forbidden indirect transitions, respectively. The Tauc plot equation is a commonly used method to analyze the optical absorption coefficient ( $\alpha$ ) against photon energy ( $h\nu$ ).

The changes in band energy for all the studied composites are shown in Fig. 4c. Based on the band gap energies ( $E_g$ ) obtained, the calculated band gap for the Cu@PC catalyst was found to be 3.05 eV. It's important to note that the band gap of Cu can vary significantly based on various factors, including the deposition method, type of support, and particle size, and can fall within the range of 2.18 to 3.50 eV.<sup>57–59</sup> The highest band gap energy of 3.15 eV for Cu/Ni<sub>2</sub>O<sub>3</sub>@PC suggests that it requires more energy for electronic transitions compared to other catalysts with lower band gap energies. The band gap energy for Ni<sub>2</sub>O<sub>3</sub>@PC composite was determined to be 2.98 eV. These





Table 2 XRD and structural parameters of the composite TeMs

Composite	Phase/phase content, %	hkl <sup>a</sup>	2θ°	d <sup>b</sup> , Å	r <sup>c</sup> , nm	FWHM <sup>d</sup>	MTs structural parameters				Amount of loaded phase, mg cm <sup>-2</sup>	R <sub>f</sub> , mg cm <sup>-2</sup> h <sup>-1</sup>
							Cell parameter <sup>e</sup> , Å	V <sub>r</sub> , Å <sup>3</sup>	Wall thickness, nm	Inner diameter, nm		
Cu@PC	Cu 100	111	43.25	2.090	32.29	0.294	a = 3.608	46.97	75.6 ± 7.4	258.9	4.18	0.108
		200	50.54	1.805	20.30	0.481						
		220	74.07	1.279	22.41	0.494						
Ni <sub>2</sub> O <sub>3</sub> @PC	Ni <sub>2</sub> O <sub>3</sub> /100	311	89.98	1.090	17.40	0.717	a = 4.634, c = 5.602	104.20	63.4 ± 2.3	293.2	5.63	70.65
		202	36.53	2.458	39.73	0.234						
		102	39.04	2.306	36.70	0.255						
Cu/Ni <sub>2</sub> O <sub>3</sub> @PC	CuNi/97.3	111	43.42	2.083	35.88	0.265	a = 3.607	46.92	103.8 ± 3.2	215.6	6.28	0.0872 (copper doping stage)
		200	50.58	1.803	27.28	0.358						
		220	74.28	1.276	37.44	0.296						
		311	89.94	1.089	36.97	0.338	a = 4.670, b = 3.411, c = 5.126, β = 99.331	80.58				
		222	95.31	1.042	49.80	0.263						
		111	38.95	2.311	31.36	0.299						

<sup>a</sup> Miller indices for corresponding planes. <sup>b</sup> Spacing between planes. <sup>c</sup> Full-width at half-maximum. <sup>d</sup> Crystal lattice parameter. <sup>e</sup> Deposition rate of the electroless metal plating.

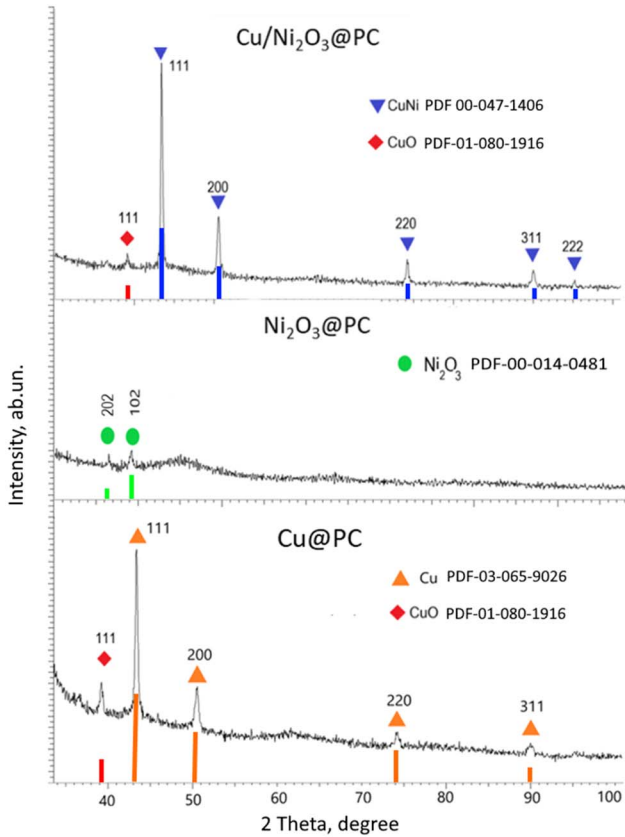


Fig. 3 X-ray diffraction patterns of Cu@PE, Ni<sub>2</sub>O<sub>3</sub>@PC, and Cu/Ni<sub>2</sub>O<sub>3</sub>@PC composites.

results suggest that the Cu/Ni<sub>2</sub>O<sub>3</sub>@PC mixed catalyst is more efficient in harnessing energy from UV irradiation to drive the decomposition process. A higher band gap energy potentially enables better utilization of UV energy, leading to increased generation of reactive species for the degradation of hazardous chemicals.<sup>45</sup>

### 3.2. Catalytic degradation of NOR antibiotic

Antibiotics are among the predominant chemicals that make water unsuitable for both human and the environment. The presence of antibiotics, including norfloxacin (NOR), in water at elevated concentrations can lead to detrimental effects, such as gastrointestinal issues and allergic reactions. Furthermore, high concentrations of antibiotics in aqueous environments can exert toxic effects on aquatic organisms, disrupting ecosystems. This disruption can impact the food chain and ultimately result in decreased biodiversity in affected water bodies.

In Fig. 5, the absorbance spectra of the NOR solution in the presence of the synthesized catalysts are depicted. The spectrum of NOR reveals a characteristic absorption peak at 275 nm. As the reaction time increases, the intensity of this absorbance peak gradually decreases for all the studied catalysts, indicating the successful degradation of NOR. The pH value is an important factor affecting the removal efficiency of NOR due to the



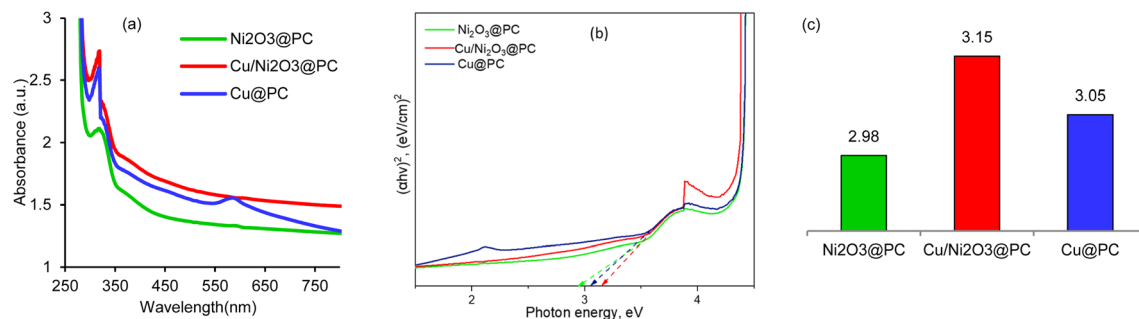


Fig. 4 The UV-vis transmission spectra (a), Tauc plot employed for the estimation of the optical band gap in the composite TeMs (b) and corresponding values of the band gap energy ( $E_g$ ) values (c).

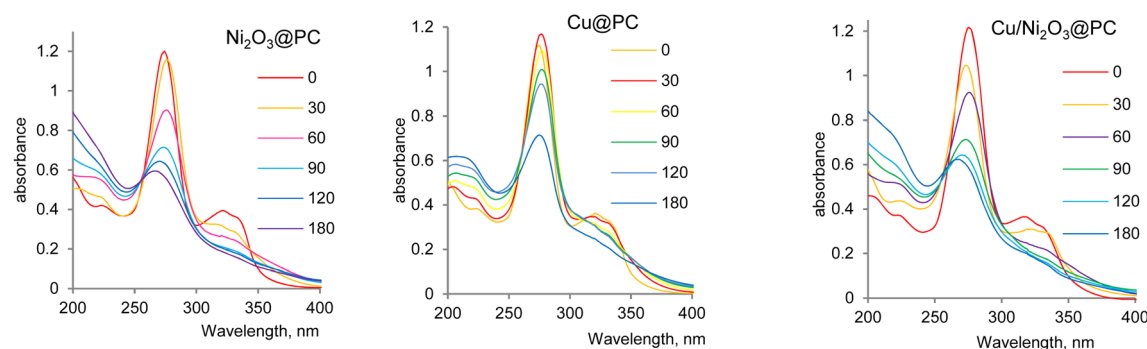


Fig. 5 Typical absorption spectra for the decomposition of NOR under UV-vis light in the presence of the studied composite membrane (NOR concentration – 10 mg L<sup>-1</sup>, temperature – 40 °C, size of the catalyst membrane – 2 × 2 cm).

chemical structure of NOR, which possesses two proton-binding sites (carboxyl and piperazinyl groups) with distinct  $pK_a$  values of 6.31 and 8.68, respectively<sup>60</sup> (Fig. 6a). As a result, the NOR molecule can exist in various forms, including cationic (NOR<sup>+</sup>), zwitterionic (NOR<sup>±</sup>), neutral (NOR<sup>0</sup>), or anionic (NOR<sup>-</sup>), depending on the pH of the solution.<sup>61,62</sup> The parameter known as pH of zero-point charge ( $pH_{zpc}$ ) was evaluated to determine the surface charge of the composites (Fig. 6b).  $pH_{PZC}$  signifies the pH at which the surface of the adsorbent or catalyst attains a state of net electrical neutrality.<sup>63</sup>

The surface charge of all the studied composites is positively charged at pH levels lower than the  $pH_{PZC}$  and becomes negatively charged at pH values beyond the  $pH_{PZC}$ . Under strong acidic conditions, all composites and NOR are positively charged. In such conditions, the intense electrostatic repulsion between like charges hinders the approach of NOR to the composite surface, resulting in reduced degradation efficiency.<sup>62</sup> In the pH range of 5–7, which is close to the first  $pK_a$  of NOR, NOR predominantly exists in its zwitterionic form, containing both concurrent positive and negative charges. This configuration promotes the attraction between the negatively

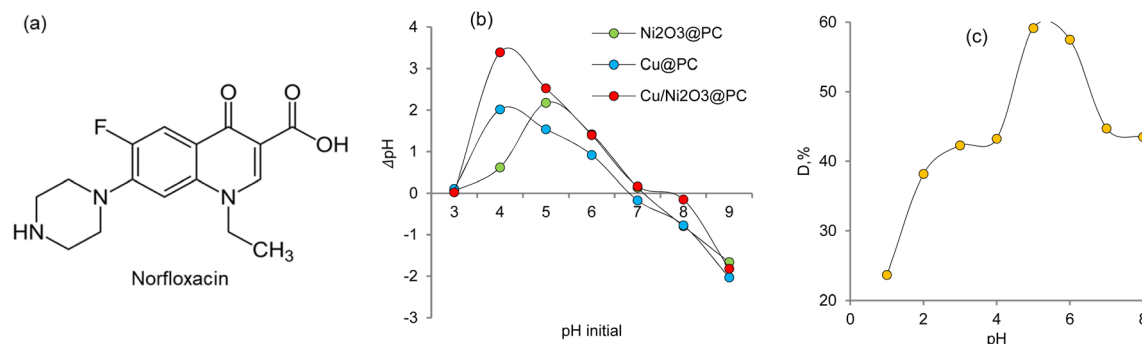


Fig. 6 The chemical structure of norfloxacin (a), the point of zero charge ( $pH_{PZC}$ ) plot for the surface of the composites (b), the effect of the initial pH of the NOR feed solution on degradation efficiency (with NOR concentration at 10 mg L<sup>-1</sup>, temperature at 40 °C Cu/Ni<sub>2</sub>O<sub>3</sub>@PC loading at 25.1 mg) (c).



charged NOR and the positively charged composite catalyst, facilitating the degradation reaction. Similar observations have been reported in previous studies.<sup>61,63</sup> This observation is in good accordance with the data presented in Fig. 6c, which demonstrates the effect of the initial pH value of the NOR solution in the presence of the Cu/Ni<sub>2</sub>O<sub>3</sub>@PC catalyst. The degradation rate increases with an increase in pH, reaching an optimal value at pH 5.0, after which it starts to decrease in the pH range of 6.0–8.0.

One of the key advantages of heterogeneous and supported catalysts is their rapid separation and recycling without significant loss in catalytic performance.<sup>64</sup> Immobilizing the active catalyst phase on a solid support, such as polymeric TeMs, offers numerous benefits, including long-term stability, simplified application, and improved catalytic performance. Flexible, chemically and mechanically stable composites based on polymeric TeMs present promising opportunities for efficient separation and potential catalyst reuse. The hollow structure of such membrane catalysts also allows for both static (bath) and dynamic (cross-flow) modes.<sup>65</sup>

In this study, the long-term stability of the synthesized composites was examined over 10 consecutive runs without any additional activation or recovery procedures (Fig. 7c). The copper based membrane catalyst significantly lost its activity after the 2-nd test cycle and could only catalyze 10% of NOR after the 10-th testing cycle. In contrast, the Ni<sub>2</sub>O<sub>3</sub>@PC catalyst maintained a more stable degradation efficiency for NOR removal throughout 10 runs, removing approximately 27% of NOR during the final test. The catalytic performance of the Cu/Ni<sub>2</sub>O<sub>3</sub>@PC mixed composite was superior compared to the single-component composite membranes. Its removal efficiency remained consistent for the first 4 runs and decreased slightly (17%) after the 6-th run, while 35% of NOR was removed in the 10-th cycle.

The photocatalytic performance of the synthesized composite membranes in NOR-containing water is demonstrated in Fig. 7a. The removal efficiencies of NOR when using Ni<sub>2</sub>O<sub>3</sub>@PC and Cu@PC reached 47.05 and 34.55%, respectively, within 180 min under UV-light exposure. Notably, the catalytic activity of the mixed composite catalyst Cu/Ni<sub>2</sub>O<sub>3</sub>@PC exceeded

that of the pristine single-component composites, achieving a removal efficiency of 59.15%. The pseudo-first-order kinetic model was employed to describe the studied reaction. The kinetic curves for the UV-induced decomposition of NOR in the presence of the studied composites (2 × 2 cm) are presented in Fig. 7b. These curves indicate that the Langmuir–Hinshelwood plots were linear, suggesting that the photodecomposition of NOR follows the pseudo-first-order reaction kinetics. Accordingly, the calculated rate constant ( $k_a$ ) for the mixed composite was determined as  $0.55 \times 10^{-2} \text{ min}^{-1}$ , while lower values of  $0.39 \times 10^{-2} \text{ min}^{-1}$  and  $0.28 \times 10^{-2} \text{ min}^{-1}$  were found for Ni<sub>2</sub>O<sub>3</sub>@PC and Cu@PC catalysts, respectively.

The observed decrease in the degradation efficiency of all studied catalysts could be attributed to the washout of the active catalytic phase from the surface of the polymer template due to the intensive agitation of the reaction mixture during catalytic experiments. To support this claim, AFM analyses of the catalysts were conducted initially and after the 10th cycle (Fig. 8a). The reduction in surface roughness (Fig. 8b) after the 10th cycle is likely due to the removal of the active catalyst nanophases from the structure over multiple runs. Previous studies have revealed that as the surface roughness increases, the catalytic activity at the membrane also increases.<sup>66,67</sup> The decrease in efficiency of NOR degradation in the catalyst membranes during repeated tests can primarily be attributed to the removal of the active catalyst phases from the structure, resulting in reduced surface roughness and, consequently, a diminished active surface area. These factors collectively contribute to decreased efficiency.

For the mixed composite membrane, the incorporation of copper into the Ni<sub>2</sub>O<sub>3</sub>@PC composite is evident in the 2D AFM images shown in Fig. 8a (right), along with the comparative  $R_a$  plot displayed in Fig. 8b. This doping process results in an increase in surface roughness. The primary factor contributing to this phenomenon is the formation of copper domains, as supported by the SEM images provided in Fig. 1c. As a result, the Cu/Ni<sub>2</sub>O<sub>3</sub>@PC surface exhibits a more uneven and irregular profile, signifying a higher surface roughness and, consequently, a greater surface area. Notably, discrete clusters of copper nanoparticles can be observed on the relatively smooth surface of membranes, in agreement with SEM analysis. In the

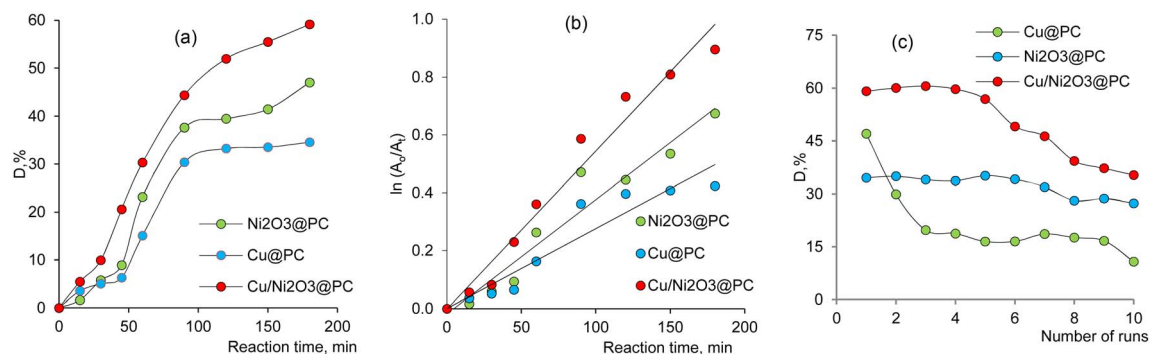


Fig. 7 The effect of contact time on NOR degradation (a), the variation of the natural logarithm of normalized concentration ( $\ln(C_0/C)$ ) as a function of UV-light irradiation time (b), and the reusability of the studied catalysts for the degradation of NOR (NOR concentration at  $10 \text{ mg L}^{-1}$ , pH at 5.0, temperature at  $40^\circ \text{C}$ , catalyst membrane size at  $2 \times 2 \text{ cm}$ ) (c).



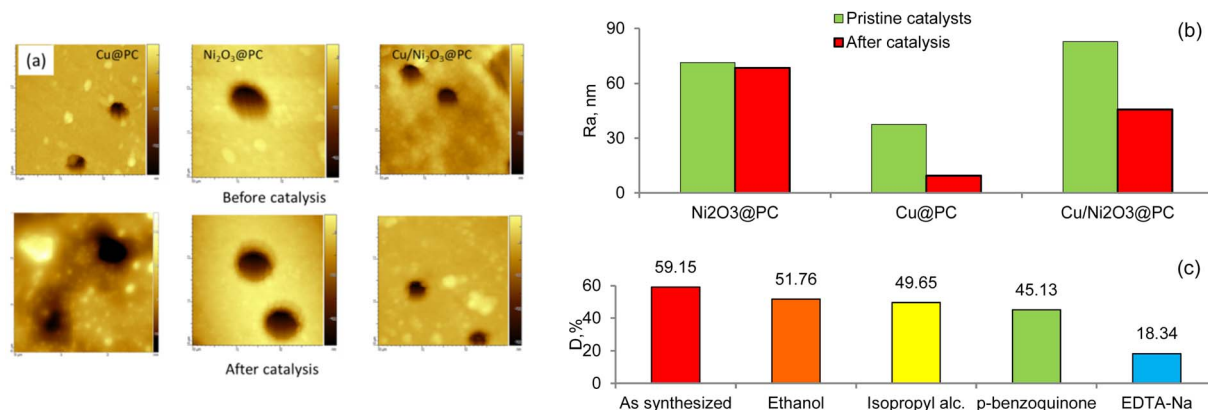


Fig. 8 AFM images of the composite catalyst surfaces before and after the 10-th run of catalytic degradation (a), featuring a scanning area of  $3 \times 3 \mu\text{m}^2$ . The corresponding values of roughness  $R_a$  (b), and a comparison of degradation efficiency of the Cu/Ni<sub>2</sub>O<sub>3</sub>@PC catalysts in the presence of different quenchers (c).

case of the Cu@PC composite, following ten cycles of testing, a substantial decrease was observed in the quantity of the active catalyst Cu phase on the sample's surface, resulting in a significant reduction (74.8%) in the  $R_a$  value. For the mixed composite membrane, the reduction in  $R_a$  was less pronounced (44.8%), although it still indicated a substantial loss of the active catalyst phases. This loss contributed to the subsequent decrease in NOR degradation efficiency. On the other hand, the reduction in  $R_a$  was minimal (9.4%) for Ni<sub>2</sub>O<sub>3</sub>@PC membrane, allowing this sample to maintain its catalytic activity almost unchanged over ten cycles (Fig. 7c). Based on these observations, it can be inferred that the doping of Cu to Ni<sub>2</sub>O<sub>3</sub> phase, as opposed to the pristine Cu phase, increases the retention of the active catalytic phase within the membrane structure. This results in an enhanced amount and surface area of the active phase during repeated use. In addition to the formation of the CuNi-based solid substitution solution (SSS) phase, all of these factors together significantly enhance the catalytic performance of the mixed composite.

### 3.3. Photocatalytic reaction mechanism

It is a well-known fact that hydroxyl radicals ( $\text{OH}^\bullet$ ), superoxide radicals ( $\text{O}_2^\bullet$ ) and holes ( $\text{h}^+$ ) are the main reactive species responsible for the degradation of different types of antibiotics, including NOR.<sup>68,69</sup> To identify the reactive species responsible for the efficient degradation of NOR, additional experiments with quenchers (isopropyl alcohol, ethanol, EDTA-Na<sub>2</sub>, *p*-benzoquinone) were carried out.<sup>70</sup> The photodegradation efficiency of the Cu/Ni<sub>2</sub>O<sub>3</sub>@PC composite in presence of different quenchers of specific reactive species is presented in Fig. 8c. The analysis of the presented data revealed that degradation ratio ( $D$ , %) was reduced in the presence of all types of quenchers. Addition of ethanol (quencher of electrons,  $\text{e}^-$ ) and isopropyl alcohol (quencher of hydroxyl radicals  $\text{OH}^\bullet$ ) decreased  $D$  value from 59.15% to 51.8% and 49.7%, respectively. A minor decrease in the photodegradation efficiency of NOR (by 5.0%) was observed after adding *p*-benzoquinone (superoxide anion radical quencher) to the NOR mixture.

Table 3 Comparison of the Cu/Ni<sub>2</sub>O<sub>3</sub>@PC catalyst and other similar composite catalysts towards the removal of NOR

Catalyst	Amount of loaded catalyst, mg	Catalyst test conditions							Ref.
		<i>T</i> , °C	NOR concentration	Light source	pH	Contact time, min	<i>D</i> %	<i>k</i> , min <sup>−1</sup>	
Bi <sub>2</sub> Sn <sub>2</sub> O <sub>7</sub> /perylene diimide	10.0	—	10.0	Visible	6.48	90	98.9	0.490	73
Fe <sub>3</sub> O <sub>4</sub> @La–BiFeO <sub>3</sub>	350.0	—	20.0	Visible	5.0	60	93.8	0.059	74
Chitosan functionalized CuO NPs	40.0	—	25.0	Sun light	—	60.0	71.9	0.010	75
Bi <sub>2</sub> WO <sub>6</sub> /Cs <sub>2</sub> AgBiBr <sub>6</sub> halide double perovskites	40.0	—	10.0	Visible	—	60	63.1		76
NH <sub>2</sub> -MIL-53(Fe/Ti) composite	20.0	—	10.0	Visible	7.5	120	84.6	0.016	77
ZnO/ZnS@biochar composite	125.0	25	25.0	UV-light	5.0	180	40.0	0.019	78
Ag <sub>2</sub> CO <sub>3</sub> /ZnFe <sub>2</sub> O <sub>4</sub> /bentonite composite	50.0	—	30.0	Visible	—	30	94.4	—	79
ZnFe <sub>2</sub> O <sub>4</sub>							39.2	—	
Biogenic Ag NPs	50.0	25	10.0	Visible	—	80	94.0	—	80
Mn:ZnS quantum dots	60.0	—	15.0	UV-light	10.0	60	86.0	0.032	81
Cu/Ni <sub>2</sub> O <sub>3</sub> @PC	25.0	40	20.0	UV-light	5.0	180	59.2	0.006	This study
Ni <sub>2</sub> O <sub>3</sub> @PC	22.5						47.0	0.004	
Cu@PC	16.7						34.6	0.003	

Notably, the addition of EDTA- $\text{Na}_2$  (quencher of holes,  $\text{h}^+$ ) to the reaction mixture significantly decreased the efficiency of the composite catalyst by threefold, indicating the oxidative nature of photodegradation reaction. This decrease in photocatalytic degradation efficiency clearly indicates that holes are the main reactive species playing an important role in the photocatalytic degradation of NOR compared to  $\text{O}_2^{\cdot-}$  and  $\text{OH}^{\cdot-}$  radicals.

The above findings align well with prior studies,<sup>70–72</sup> suggesting that, among all the possible photogenerated reactive species, holes  $\text{h}^+$  appear to be the key active species responsible for the photocatalytic degradation of NOR by the composite TeMs.

The overall results from the present study are compared to the results obtained in previous studies in Table 3. It's important to note that direct comparison of catalytic activities of different catalysts listed in the table is difficult due to variations in preparation and test conditions, synthesis methods, and techniques for determining degradation efficiency. Nevertheless, the comparative data indicate that composite catalyst based on  $\text{Ni}_2\text{O}_3$  and mixed composite with SSS of CuNi, derived from it, provide comparable values of degradation efficiency for NOR removal compared to existing alternatives, making them promising materials for the effective removal of antibiotics from aqueous media.

## 4. Conclusion

This study explores the synthesis and characterization of composite membranes designed for the efficient removal of antibiotics, specifically norfloxacin (NOR), from aqueous media. Electroless deposition techniques were employed to create  $\text{Ni}_2\text{O}_3@\text{PC}$  and  $\text{Cu}@\text{PC}$  composite membranes, while a mixed composite,  $\text{Cu}/\text{Ni}_2\text{O}_3@\text{PC}$ , was obtained through a galvanic replacement approach by doping  $\text{Ni}_2\text{O}_3@\text{PC}$  with copper, resulting in a substitutional solid solution CuNi phase (97%) and a minor CuO phase (2.7%). The structural and catalytic properties of these membranes were comprehensively examined. Notably, XRD analysis revealed the presence of a face-centered cubic structure of the Ni-Cu alloy in  $\text{Cu}/\text{Ni}_2\text{O}_3@\text{PC}$  composite.

Assessment of the optical absorption properties using UV-Vis diffuse reflectance spectroscopy (DRS) led to the calculation of band gap energies for all composites.  $\text{Cu}/\text{Ni}_2\text{O}_3@\text{PC}$  exhibited the highest band gap energy of 3.15 eV, positioning it as an effective catalyst for harnessing UV energy in NOR degradation. Photocatalytic degradation experiments revealed that the mixed  $\text{Cu}/\text{Ni}_2\text{O}_3@\text{PC}$  composite achieved a remarkable removal efficiency of 59.15% within 180 minutes under UV-light, surpassing the performance of other composites. The photocatalytic reaction kinetics followed a pseudo-first-order model, with  $\text{Cu}/\text{Ni}_2\text{O}_3@\text{PC}$  displaying a significantly higher rate constant ( $k_a$ ) of  $0.55 \times 10^{-2} \text{ min}^{-1}$ . Moreover, evaluation of the long-term stability of the composite membranes revealed that the mixed composite maintained its catalytic activity throughout the first 4 runs, and exhibited enhanced activity in subsequent cycles, outperforming the other catalysts. This stability, coupled with superior performance, positions the mixed composite as

a highly promising catalyst for prolonged and repeated use in wastewater treatment applications. The reduction in reaction efficiency can be attributed to the substantial washout of catalytically active particles from the composite surface, as validated by AFM analysis. The photocatalytic reaction mechanism investigation identified holes ( $\text{h}^+$ ) as the primary reactive species responsible for the photocatalytic degradation of NOR.

The presence of both active phases (CuNi and CuO) in the mixed composite membrane catalyst, particularly at the interfaces, is speculated to generate a synergistic catalytic effect during the photodegradation of NOR when employing  $\text{Cu}/\text{Ni}_2\text{O}_3@\text{PC}$  composite. In summary, the composite membranes, particularly  $\text{Cu}/\text{Ni}_2\text{O}_3@\text{PC}$ , offer a practical and efficient means of removing antibiotics like NOR from aqueous media. The mixed composite's structural characteristics, improved optical absorption, ease of use, simple fabrication, and high photocatalytic performance position it as a promising alternative for addressing water pollution challenges associated with antibiotic contamination.

## Abbreviations

NPs	Nanoparticles
XRD	X-ray diffraction
SEM	Scanning electron microscopy
EDX	Energy dispersive X-ray analysis
NOR	Norfloxacin
AFM	Atomic force microscopy
FWHM	Full width at half maximum
SSS	Solid substitution solution
DC	Degree of crystallinity (%)
$L$	Average crystallite size (nm)
$R_a$	Roughness
RS	Reactive species

## Author contributions

Conceptualization, A. A. M. and M. B.; methodology, D. T. N.; validation, A. A. M. and D. T. N.; formal analysis, D. T. N.; investigation, D. T. N.; writing-original draft preparation, D. T. N.; writing-review and editing, M. B. and D. T. N.; supervision, A. A. M. and M. B.; project administration D. T. N.; funding acquisition, D. T. N. All authors have read and agreed to the published version of the manuscript.

## Conflicts of interest

The authors declare no conflict of interest.

## Acknowledgements

The research titled "Synthesis of multicomponent composite catalysts and study of their properties in reactions of photocatalytic decomposition of various classes of antibiotics" (grant IRN AP14971803) was funded by the Ministry of Science and Higher Education of the Republic of Kazakhstan.



## References

- 1 A. Machin, K. Fontánez, J. Duconge, M. C. Cotto, F. I. Petrescu, C. Moran and F. Márquez, *Catalysts*, 2022, **12**, 1–17.
- 2 X. Zhou, G. J. P. Cuasquer, Z. Li, H. P. Mang and Y. Lv, *Environ. Int.*, 2021, **146**, 106280.
- 3 Y. Ghaffari, S. Beak, J. Bae, M. Saifuddin and K. S. Kim, *Catalysts*, 2022, **12**, 424.
- 4 M. Patel, R. Kumar, K. Kishor, T. Mlsna, C. U. Pittman and D. Mohan, *Chem. Rev.*, 2019, **119**, 3510–3673.
- 5 K. Kulik, A. Lenart-Boroń and K. Wyrzykowska, *Water*, 2023, **15**, 975.
- 6 M. González-Pleiter, S. Gonzalo, I. Rodea-Palomares, F. Leganés, R. Rosal, K. Boltes, E. Marco and F. Fernández-Piñas, *Water Res.*, 2013, **47**, 2050–2064.
- 7 D. G. J. Larsson and C.-F. Flach, *Nat. Rev. Microbiol.*, 2022, **20**, 257–269.
- 8 W. Wang, Y. Weng, T. Luo, Q. Wang, G. Yang and Y. Jin, *Toxics*, 2023, **11**, 185.
- 9 S. Bhatt and S. Chatterjee, *Environ. Pollut.*, 2022, **315**, 120440.
- 10 G. Rytwo and A. L. Zelkind, *Catalysts*, 2021, **12**, 24.
- 11 T. D. M. Pham, Z. M. Ziora and M. A. T. Blaskovich, *Medchemcomm*, 2019, **10**, 1719–1739.
- 12 M. L. Corrado, W. E. Struble, C. Peter, V. Hoagland and J. Sabbaj, *Am. J. Med.*, 1987, **82**, 22–26.
- 13 A. Talebi Bezmin Abadi, A. A. Rizvanov, T. Haertlé and N. L. Blatt, *Bionanoscience*, 2019, **9**, 778–788.
- 14 A. Ashiq, M. Vithanage, B. Sarkar, M. Kumar, A. Bhatnagar, E. Khan, Y. Xi and Y. S. Ok, *Environ. Res.*, 2021, **197**, 111091.
- 15 Z.-Y. Lu, Y.-L. Ma, J.-T. Zhang, N.-S. Fan, B.-C. Huang and R.-C. Jin, *J. Water Process Eng.*, 2020, **38**, 101681.
- 16 M. Ortúzar, M. Esterhuizen, D. R. Olicón-Hernández, J. González-López and E. Aranda, *Front. Microbiol.*, 2022, **13**, 869332, DOI: [10.3389/fmicb.2022.869332](https://doi.org/10.3389/fmicb.2022.869332), <https://www.frontiersin.org/articles/10.3389/fmicb.2022.869332/full>.
- 17 K. Samal, S. Mahapatra and M. Hibzur Ali, *Energy Nexus*, 2022, **6**, 100076.
- 18 M. Z. Akbari, Y. Xu, Z. Lu and L. Peng, *Environ. Adv.*, 2021, **5**, 100111.
- 19 P. Kumari and A. Kumar, *Results in Surfaces and Interfaces*, 2023, **11**, 100122.
- 20 H. Liu, C. Wang and G. Wang, *Chem.-An Asian J.*, 2020, **15**, 3239–3253.
- 21 M. Chauhan, V. K. Saini and S. Suthar, *J. Porous Mater.*, 2020, **27**, 383–393.
- 22 T. X. Bui and H. Choi, *J. Hazard. Mater.*, 2009, **168**, 602–608.
- 23 B. Sáenz-Roblero, J. E. Durán, M. Masís-Mora, D. Ramírez-Morales and C. E. Rodríguez-Rodríguez, *J. Water Process Eng.*, 2020, **37**, 101461.
- 24 H. Ayoub, T. Roques-Carmes, O. Potier, B. Koubaisy, S. Pontvianne, A. Lenouvel, C. Guignard, E. Mousset, H. Poirot, J. Toufaily and T. Hamieh, *Environ. Sci. Pollut. Res.*, 2018, **25**, 34950–34967.
- 25 A. L. Kozlovskiy, D. I. Shlimas, A. E. Shumskaya, E. Y. Kaniukov, M. V. Zdorovets and K. K. Kadyrzhanov, *Phys. Met. Metallogr.*, 2017, **118**, 164–169.
- 26 M. P. Salinas-Quezada, D. A. Crespo-Yapur, A. Cano-Marquez and M. Videia, *Fuel Cells*, 2019, **19**, 587–593.
- 27 F. Franceschini and I. Taurino, *Phys. Med.*, 2022, **14**, 100054.
- 28 A. L. Kozlovskiy, I. V. Korolkov, G. Kalkabay, M. A. Ibragimova, A. D. Ibrayeva, M. V. Zdorovets, V. S. Mikulich, D. V. Yakimchuk, A. E. Shumskaya and E. Y. Kaniukov, *J. Nanomater.*, 2017, **2017**, 1–9.
- 29 A. A. Mashentseva, M. A. Ibragimova, S. B. Akhmetova, A. L. Kozlovskiy, M. V. Zdorovets and Z. T. Amirkhanova, *Chem. Pap.*, 2020, **74**(7), 2189–2199.
- 30 Q.-T. Nguyen, T.-G. Le, P. Bergonzo and Q.-T. Tran, *Appl. Sci.*, 2022, **12**, 2614.
- 31 F. Muench, M. Oezaslan, M. Rauber, S. Kaserer, A. Fuchs, E. Mankel, J. Brötz, P. Strasser, C. Roth and W. Ensinger, *J. Power Sources*, 2013, **222**, 243–252.
- 32 S. M. Popescu, A. J. Barlow, S. Ramadan, S. Ganti, B. Ghosh and J. Hedley, *ACS Appl. Mater. Interfaces*, 2016, **8**, 31359–31367.
- 33 D. Balarak and F. K. Mostafapour, *Indones. J. Chem.*, 2019, **19**, 211.
- 34 T. Çayır Tasdemirici, *Chem. Phys. Lett.*, 2020, **738**, 136884.
- 35 S. Agrohiya, S. Dahiya, P. K. Goyal, I. Rawal, A. Ohlan, R. Punia and A. S. Maan, *ECS Sensors Plus*, 2022, **1**, 043601.
- 36 V. Gowthami, M. Meenakshi, N. Anandhan and C. Sanjeeviraja, *AIP Conf. Proc.*, 2014, 884–886.
- 37 L. Bai, *Sci. Eng. Compos. Mater.*, 2019, **26**, 255–260.
- 38 L. S. Altynbaeva, M. Barsbay, N. A. Aimanova, Z. Y. Jakupova, D. T. Nurpeisova, M. V. Zdorovets and A. A. Mashentseva, *Nanomaterials*, 2022, **12**, 1724.
- 39 N. Parmanbek, S. D. Sütekin, M. Barsbay, N. A. Aimanova, A. A. Mashentseva, A. N. Alimkhanova, A. M. Zhumabayev, A. Yanevich, A. A. Almanov and M. V. Zdorovets, *RSC Adv.*, 2023, **13**, 18700–18714.
- 40 A. A. Mashentseva, N. A. Aimanova, N. Parmanbek, L. S. Altynbaeva and D. T. Nurpeisova, *Bull. Karaganda Univ., Chem. Ser.*, 2022, **107**, 227–238.
- 41 A. A. Mashentseva, D. B. Borgekov, D. T. Niyazova and M. V. Zdorovets, *Pet. Chem.*, 2015, **55**, 810–815.
- 42 A. A. Mashentseva, A. L. Kozlovskiy and M. V. Zdorovets, *Mater. Res. Express*, 2018, **5**, 065041.
- 43 D. Borgekov, A. Mashentseva, S. Kislitsin, A. Kozlovskiy, A. Russakova and M. Zdorovets, *Acta Phys. Pol., A*, 2015, **128**, 871–875.
- 44 F. T. L. Muniz, M. A. R. Miranda, C. Morilla dos Santos and J. M. Sasaki, *Acta Crystallogr., Sect. A: Found. Adv.*, 2016, **72**, 385–390.
- 45 N. Parmanbek, S. D. Sütekin, M. Barsbay, N. A. Aimanova, A. A. Mashentseva, A. N. Alimkhanova, A. M. Zhumabayev, A. Yanevich, A. A. Almanov and M. V. Zdorovets, *RSC Adv.*, 2023, **13**, 18700–18714.
- 46 A. A. Mashentseva, N. Seitzhappar, M. Barsbay, N. A. Aimanova, A. N. Alimkhanova, D. A. Zheltov,



- A. M. Zhumabayev, B. S. Temirgaziev, A. A. Almanov and D. T. Sadyrbekov, *RSC Adv.*, 2023, **13**, 26839–26850.
- 47 L. S. Altynbaeva, A. A. Mashentseva, N. A. Aimanova, D. A. Zheltov, D. I. Shlimas, D. T. Nurpeisova, M. Barsbay, F. U. Abuova and M. V. Zdorovets, *Membranes*, 2022, **12**(10), 1724.
- 48 C. Yang, Q. B. Zhang and A. P. Abbott, *Electrochem. commun.*, 2016, **70**, 60–64.
- 49 Y. Hong, S. Venkateshalu, S. Jeong, G. M. Tomboc, J. Jo, J. Park and K. Lee, *Bull. Korean Chem. Soc.*, 2023, **44**, 4–22.
- 50 H. Cheng, C. Wang, D. Qin and Y. Xia, *Acc. Chem. Res.*, 2023, **56**, 900–909.
- 51 N. M. Vuong, N. M. Hieu, H. N. Hieu, H. Yi, D. Kim, Y.-S. Han and M. Kim, *Sens. Actuators, B*, 2014, **192**, 327–333.
- 52 K. Chung, J. Bang, A. Thacharon, H. Y. Song, S. H. Kang, W.-S. Jang, N. Dhull, D. Thapa, C. M. Ajmal, B. Song, S.-G. Lee, Z. Wang, A. Jetybayeva, S. Hong, K. H. Lee, E. J. Cho, S. Baik, S. H. Oh, Y.-M. Kim, Y. H. Lee, S.-G. Kim and S. W. Kim, *Nat. Nanotechnol.*, 2022, **17**, 285–291.
- 53 A. A. Mashentseva, M. Barsbay, M. V. Zdorovets, D. A. Zheltov and O. Güven, *Nanomaterials*, 2020, **10**, 1552.
- 54 I. V. Korolkov, O. Güven, A. A. Mashentseva, A. B. Atıcı, Y. G. Gorin, M. V. Zdorovets and A. A. Taltenov, *Radiat. Phys. Chem.*, 2017, **130**, 480–487.
- 55 P. R. Thombal, R. S. Thombal and S. S. Han, *RSC Adv.*, 2020, **10**, 474–481.
- 56 M. Thuyet-Nguyen and J.-C. Kim, *Arch. Metall. Mater.*, 2019, **64**(3), 893–898.
- 57 M. M. Shehata, A. M. Abdelreheem, S. A. Waly and A. H. Ashour, *J. Inorg. Organomet. Polym. Mater.*, 2017, **27**, 720–727.
- 58 N. Parmanbek, N. A. Aimanova, A. A. Mashentseva, M. Barsbay, F. U. Abuova, D. T. Nurpeisova, Z. Y. Jakupova and M. V. Zdorovets, *Membranes*, 2023, **13**(7), 659.
- 59 J. J. Mohindroo, U. K. Garg and A. K. Sharma, *AIP Conf. Proc.*, 2016, **1728**, 020534.
- 60 X. Li, Y. Hu, D. She and W.-B. Shen, *Sustainability*, 2020, **12**, 3986.
- 61 W. Yang, Y. Lu, F. Zheng, X. Xue, N. Li and D. Liu, *Chem. Eng. J.*, 2012, **179**, 112–118.
- 62 M. Chen and W. Chu, *Ind. Eng. Chem. Res.*, 2012, **51**, 4887–4893.
- 63 N. S. Sulaiman, M. H. Mohamad Amini, M. Danish, O. Sulaiman, R. Hashim, S. Demirel and G. K. Demirel, *Materials*, 2022, **15**, 5117.
- 64 M. Miceli, P. Frontera, A. Macario and A. Malara, *Catalysts*, 2021, **11**, 591.
- 65 A. A. Mashentseva and M. V. Zdorovets, *Pet. Chem.*, 2019, **59**, 552–557.
- 66 I. Kim, G. Park and J. J. Na, *Int. J. Heat Mass Transfer*, 2019, **138**, 916–922.
- 67 A. A. Mashentseva and M. V. Zdorovets, *Nucl. Instrum. Methods Phys. Res. B: Beam Interact. Mater. At.*, 2020, **472**, 53–58.
- 68 H. Yu, F. Chen, L. Ye, H. Zhou and T. Zhao, *J. Mater. Sci.*, 2019, **54**, 10191–10203.
- 69 M. Pavel, C. Anastasescu, R.-N. State, A. Vasile, F. Papa and I. Balint, *Catalysts*, 2023, **13**, 380.
- 70 S. Kar, S. Ibrahim, T. Pal and S. Ghosh, *ChemistrySelect*, 2020, **5**, 54–60.
- 71 G. Zhang, Y. Xue, Q. Wang, P. Wang, H. Yao, W. Zhang, J. Zhao and Y. Li, *Chemosphere*, 2019, **230**, 406–415.
- 72 X.-J. Wen, C.-G. Niu, D.-W. Huang, L. Zhang, C. Liang and G.-M. Zeng, *J. Catal.*, 2017, **355**, 73–86.
- 73 N. Yin, H. Chen, X. Yuan, Y. Zhang, M. Zhang, J. Guo, Y. Zhang, L. Qiao, M. Liu and K. Song, *J. Hazard. Mater.*, 2022, **436**, 129317.
- 74 Z. Shan, F. Ma, M. Xu, X. Shan, L. Shan, C. Cui and H. Guo, *Chem. Eng. J.*, 2023, **466**, 143229.
- 75 M. Ganeshbabu, J. S. Priya, G. M. Manoj, N. P. N. Puneeth, C. Shobana, H. Shankar and R. K. Selvan, *Int. J. Biol. Macromol.*, 2023, **253**, 127027.
- 76 H. Zhang, X. Ji, H. Xu, R. Zhang, Y. Li and Q. Chen, *J. Alloys Compd.*, 2023, **968**, 172132.
- 77 W. Gao, F. Wang, M. Ou, Q. Wu, L. Wang, H. Zhu, Y. Li, N. Kong, J. Qiu, S. Hu and S. Song, *J. Environ. Chem. Eng.*, 2023, **11**, 111050.
- 78 W. Liu, T. He, Y. Wang, G. Ning, Z. Xu, X. Chen, X. Hu, Y. Wu and Y. Zhao, *Sci. Rep.*, 2020, **10**, 11903.
- 79 Z. Huang, X. Qiu, D. Chen, X. Wu, S. Zhang and P. Zhu, *Opt. Mater.*, 2023, **143**, 114153.
- 80 K. Kanagamani, P. Muthukrishnan, K. Shankar, A. Kathiresan, H. Barabadi and M. Saravanan, *J. Clust. Sci.*, 2019, **30**, 1415–1424.
- 81 J. Patel, A. K. Singh and S. A. C. Carabineiro, *Nanomaterials*, 2020, **10**, 964.

